

Controlling photonic spin Hall effect by a symmetric hyperbolic metamaterial waveguide

Mingxiang Gao

Wuhan University of Technology

Wenqiong Zhang

Wuhan University of Technology

Bin Guo (✉ binguo@whut.edu.cn)

Wuchang University of Technology

Research Article

Keywords: photonic spin Hall effect, hyperbolic metamaterial, transfer matrix method, reflectivity, transverse shift

Posted Date: April 26th, 2021

DOI: <https://doi.org/10.21203/rs.3.rs-452417/v1>

License:   This work is licensed under a Creative Commons Attribution 4.0 International License.

[Read Full License](#)

Controlling photonic spin Hall effect by a symmetric hyperbolic metamaterial waveguide

Ming-Xiang Gao, Wen-Qiong Zhang, Bin Guo*

Department of Physics, Wuhan University of Technology, Wuhan 430070, China

(Dated: April 9, 2021)

We investigate the photonic spin Hall effect (PSHE) in a symmetrical hyperbolic metamaterial (HMM) waveguide, which is constructed as an HMM/metal/HMM sandwich structure. We consider both type I and type II HMM in the study. We confirm that the structure of alternating sub-wavelength of plasma and dielectric or the structure of embedding plasma into a host dielectric matrix can display effective dielectric, effective metal, type I and II HMM under different wavelength ranges and different plasma fill fraction. This enable us to simultaneously realize type I and type II HMM. We show that the reflectivity ration $|r_s/r_p|$, directly related to transverse shifts generated by PSHE, greatly depends on the type and the thickness of HMM. Moreover, we find that the horizontal PSHE shifts are enhanced several times, especially in type I structure; while the vertical PSHE shifts are significantly suppressed in both type I and II structure. By making the effect of metal type and thickness analysis, we further show that the impacts of these two factors on PSHE shifts are mainly subject to HMM thickness.

Keywords: photonic spin Hall effect, hyperbolic metamaterial, transfer matrix method, reflectivity, transverse shift

I. INTRODUCTION

When a Gaussian beam is reflected or transmitted at a refractive index gradient interface, the left and right-handed circularly polarized components split and yield transverse shift. This interesting electromagnetic phenomenon named the photonic spin Hall effect (PSHE) has attracted extensive interest and has been widely studied due to its worth seeing applications in spin-controlled nano-photonic devices [1–4]. However, the spin-orbit coupling, an essential physical mechanism of PSHE, is very weak, which results in a slight PSHE [5]. Therefore, the corresponding spin-splitting shifts generated by PSHE are tiny and always at the sub-wavelength scale. This brings us great challenges to observe the PSHE shifts and advance the potential applications of PSHE. Although it was recently developed by Hosten and Kwiat [5] that the weak measurements method [6–8] is successfully employed to characterize the PSHE shifts, enhancing and controlling PSHE shifts is still an important issue. Many various architectures have been proposed to enhance PSHE shifts, such as different material interfaces [9–12], optical systems [13–15], metasurfaces [16–18], photonic crystals [19–22], metamaterials [23–33], and other systems [34–42].

Among the above means to enhancing and controlling PSHE shifts, using metamaterial [23–33] is the most attractive way owing to its excellent tunable features and superior properties. Hyperbolic metamaterial (HMM) is a kind of metamaterials and can be assumed as a uniaxial metalcrystal whose effective permittivities for different polarizations have different signs [43, 44]. HMM can be realized by a sub-wavelength layered metal-dielectric

structure with an extremely anisotropic dielectric tensor $diag(\varepsilon_{\parallel}, \varepsilon_{\parallel}, \varepsilon_{\perp})$. Generally, the isofrequency surface of HMM is hyperbolic ($\varepsilon_{\parallel}\varepsilon_{\perp} < 0$) when the uniaxial components of the dielectric tensor are of opposite signs. There are two possibilities of HMM. We classify these two possibilities according to the number of negative components of the dielectric tensor as type I ($\varepsilon_{\parallel} > 0$, and $\varepsilon_{\perp} < 0$) and type II ($\varepsilon_{\parallel} < 0$, and $\varepsilon_{\perp} > 0$). Recently, HMMs are introduced into the researches of PSHE because of their higher degree of controlling the propagation of electromagnetic waves. However, almost all studies focus on by using type I HMM to tune PSHE shifts [23–33]. The reports of using type II HMM to enhance or control PSHE shifts have rarely been investigated [32, 33]. The enhanced PSHE shifts in horizontally placed type I HMM (parallel to the normal vector of the substrate) occur at an extremely low efficiency below 0.01 [32], thereby inhibiting practical applications. Fortunately, in our previous work, we find that the horizontal PSHE shifts can be enhanced by more than twenty times in a prism-coupling waveguide with type II HMM. This brings us a new way to enhancing or controlling PSHE shifts. Therefore, we propose a symmetric HMM waveguide to explore how the PSHE shifts behave. The waveguide is typically one enclosed metal sheet cladded by two same HMM layers. As a comparison, we consider both type I and type II HMM waveguides in the study. We discuss how the type and thickness of HMM affect the PSHE shifts. Moreover, we further show the effect of the metal type and thickness on the features of PSHE shifts.

The outline of the paper is organized as follows. In Sec. II, we first introduce our model and then present the corresponding formulas of calculating transverse shifts of PSHE. The results and discussions are presented in Sec. III. Finally, we give a summary in Sec. IV.

* binguo@whut.edu.cn (B. Guo)

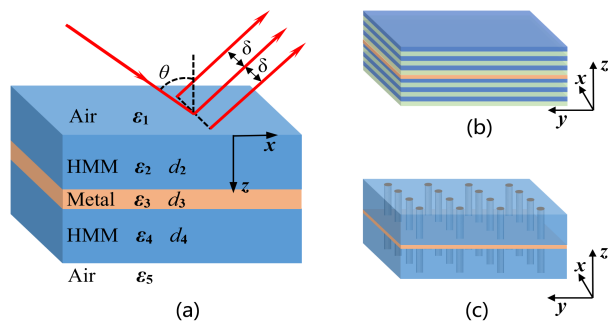


FIG. 1. (Color online) (a) Schematic diagram of PSHE of the reflected light in the symmetric HMM waveguide. (b) HMM engineered through multilayer realization consists of alternating subwavelength layers of plasma and dielectric. (c) HMM engineered through embedding plasma in a host dielectric matrix.

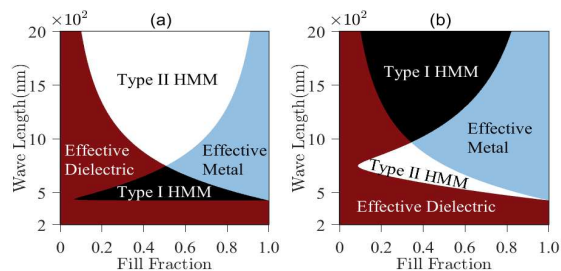


FIG. 2. (Color online) The engineered composite can behave as an effective dielectric, effective metal, type I HMM or type II HMM depending on the wavelength and fill fraction of the plasma. Optical phase diagrams for (a) one-dimensional HMM, and (b) Two-dimensional HMM.

II. MODEL AND FORMULAS

We study the PSHE of reflected light in a symmetrical HMM waveguide, which schematic diagram of the engineered structure is shown in Fig. 1(a). The geometrical illustration of the transverse shifts of the beam upon reflection of HMM waveguide is also shown in Fig. 1. The engineering of HMM waveguide is represented as Air/HMM/Metal/HMM/Air, which the relative permittivities are denoted as $\epsilon_1, \epsilon_2, \epsilon_3, \epsilon_4$, and ϵ_5 , respectively, and d_2, d_3 , and d_4 are the thickness of the HMM layer, metal sheet, and HMM layer, respectively. Because the HMM waveguide is purely proposed for symmetric structure, the thicknesses and the kinds of these two HMM layers are the same, which means $d_2 = d_4$. We herein use a quantity d to signify d_2 and d_4 . The permeabilities of all layers are supposed to be non-magnetic media with $\mu = 1$ in the study.

The fundamental property of the HMM is that it has dielectric properties in one direction but metallic properties in an orthogonal direction. The HMM layer can be viewed as uniaxial metacrystals with an extremely

anisotropic dielectric tensor $\epsilon_i = \text{diag}(\epsilon_{\parallel}, \epsilon_{\parallel}, \epsilon_{\perp})$, ($i = 2, 4$), which is extremely anisotropic and cannot be observed in nature at optical frequencies. Notably, the HMM considered in the study is horizontally placed, which is parallel to the normal vector of the substrate. It is well known that there are two prominent methods to engineer practical hyperbolic media. Herein, we provide the details for the theoretical models of an effective medium. The first method employed for accomplishing the HMM is a one-dimensional structure, which can be realized for a multilayer system with alternating plasma and dielectric layers, shown in Fig. 1(b). The second method adopted for realizing the HMM is a two-dimensional structure, which can be created by embedding microplasma in a host dielectric matrix, as seen in Fig. 1(c). The permittivity tensor components, ϵ_{\parallel} and ϵ_{\perp} , can be determined by employing the generalized Maxwell-Garnett approach [45–47]. Their specific expressions can be found in [33]. Herein, we assume that the dielectric function of plasma is described by the Drude model, i.e., $\epsilon_p = 1 - \omega_p^2/(\omega(\omega + i\gamma))$, where ω_p is the plasma frequency, ω is the frequency of incidence, and γ denotes the collision in plasma.

Figure 2 shows the the optical phase diagram for the HMM where the effective medium response is plotted with the incident wavelength and the fill fraction of plasma. The parameters are chosen as $\omega_p = 1.5 * 2\pi c/\lambda_0$, and $\gamma = 0.1 * 2\pi c/\lambda_0$, where λ_0 is the work wavelength and c is the speed of the vacuum. The background dielectric made from metamaterial is chosen as SiO_2 with the dielectric constant $\epsilon = 2.1$. It is observed that there are four regions of the effective medium response which correspond to different forms of the engineered metamaterials. The brown regions denote the effective dielectric ($\epsilon_{\parallel} > 0$ and $\epsilon_{\perp} > 0$), the sky blue regions denote the effective metal ($\epsilon_{\parallel} < 0$ and $\epsilon_{\perp} < 0$), the black regions denote the Type I HMM ($\epsilon_{\parallel} > 0$ and $\epsilon_{\perp} < 0$), and the white regions denote the Type II HMM ($\epsilon_{\parallel} < 0$ and $\epsilon_{\perp} > 0$), respectively. From Fig. 2, we can conclude that we can simultaneously realize Type I HMM and Type II HMM both in one-dimensional and two-dimensional structures if we choose the apposite incident wavelength and plasma filling fraction. For example, taking the case of plasma fill fraction $\rho = 0.5$, type I HMM can be created in the regions of $\lambda \in (424, 744)\text{nm}$ while type II HMM also can be confirmed when $\lambda > 752\text{nm}$ when engineered for one-dimensional structure. Besides, when considered the two-dimensional structure, the type I HMM can be realized when $\lambda > 1142\text{nm}$ while the type II HMM can be created in the region of $\lambda \in (555, 751)\text{nm}$. Similar results are also confirmed by Cortes et.al [47].

It is known that the transverse shift generated by PSHE has a direct relationship with the reflectivity under different polarizations [20, 40]. Thus, the reflection coefficient at different polarization matures the primary consideration. We assume that a monochromatic Gaussian beam impinges from the air to the designed HMM waveguide, seeing in Fig. 1(a). The Gaussian beam can

be characterized by the angular spectrum theory, which is expressed as

$$\tilde{E}_i = \frac{w_0}{\sqrt{2\pi}} \exp \left[-\frac{w_0^2(k_x^2 + k_y^2)}{4} \right], \quad (1)$$

where w_0 is the Gaussian beam waist, k_x and k_y are the wave vector components in the x and y directions, respectively.

The reflected and incident light can be correlated by reflection coefficients, which can be signified by matching the boundary condition as follows:

$$\begin{bmatrix} \tilde{E}_r^H \\ \tilde{E}_r^V \end{bmatrix} = \begin{bmatrix} r_p & \frac{k_y \cot \theta_i (r_p + r_s)}{k_0} \\ -\frac{k_y \cot \theta_i (r_p + r_s)}{k_0} & r_s \end{bmatrix} \begin{bmatrix} \tilde{E}_i^H \\ \tilde{E}_i^V \end{bmatrix}, \quad (2)$$

where $k_0 = 2\pi/\lambda$, H and V represent the horizontal and vertical polarization, respectively. Herein, $r_{p,s}$ are the Fresnel reflection coefficients, which can be determined using the transfer matrix method (TMM). The beam is incident from the air onto the HMM waveguide along z -axis at a specified angle θ . By using the TMM, the electric and magnetic fields at any position z and $z + \Delta z$ in the same layer can be related via a transfer matrix [48]

$$m_j = \begin{bmatrix} \cos(k_{jz}d_j) & -\frac{i}{\gamma_j} \sin(k_{jz}d_j) \\ i\gamma_j \sin(k_{jz}d_j) & \cos(k_{jz}d_j) \end{bmatrix}, \quad (j = 1, 2, 3, 4, 5), \quad (3)$$

where k_{jz} is the z component wave vector in the layer. The expressions of k_{jz} have different forms for metal layer and HMM layer. For metal layer, whether TE-mode or TM-mode, $k_{jz} = k_0\sqrt{\varepsilon_j - \varepsilon_1 \sin^2 \theta}$. However, for HMM layer, $k_{jz} = k_0\sqrt{\varepsilon_{\parallel j} - \varepsilon_1 \sin^2 \theta}$ for TE-mode, and $k_{jz} = k_0\sqrt{\varepsilon_{\parallel j} - \frac{\varepsilon_{\perp j}}{\varepsilon_{\perp j}} \varepsilon_1 \sin^2 \theta}$ for TM-mode. Besides, for metal layer, $\gamma_j = z_0\sqrt{\varepsilon_j} \sqrt{1 - \varepsilon_1 \sin^2 \theta / \varepsilon_j}$ for TE-mode, and $\gamma_j = \frac{1}{z_0} \sqrt{1 - \varepsilon_1 \sin^2 \theta / \varepsilon_j} / \sqrt{\varepsilon_j}$ for TM-mode. Moreover, for HMM layer, $\gamma_j = z_0\sqrt{\varepsilon_{\parallel j}} \sqrt{1 - \varepsilon_1 \sin^2 \theta / \varepsilon_{\parallel j}}$ for TE-mode, and $\gamma_j = \frac{1}{z_0} \sqrt{1 - \varepsilon_1 \sin^2 \theta / \varepsilon_{\parallel j}} / \sqrt{\varepsilon_{\parallel j}}$ for TM-mode. Herein, $z_0 = (\mu_0/\varepsilon_0)^{1/2}$ is the impedance of free space, where μ_0 and ε_0 are the permittivity and permeability in the free space, respectively.

The total transmission matrix is usually accomplished by multiplying a single layer transmission matrix, which can be presented by the following formula

$$M = \prod_{i=1}^N m_j = \begin{bmatrix} m_{11} & m_{12} \\ m_{21} & m_{22} \end{bmatrix}. \quad (4)$$

Hence, the reflection coefficients $r_{p,s}$ at different polarization can be obtained as

$$r = \frac{m_{11}\gamma_0 + m_{12}\gamma_0\gamma_{n+1} - m_{21} - m_{22}\gamma_0}{m_{11}\gamma_0 + m_{12}\gamma_0\gamma_{n+1} + m_{21} + m_{22}\gamma_0}, \quad (5)$$

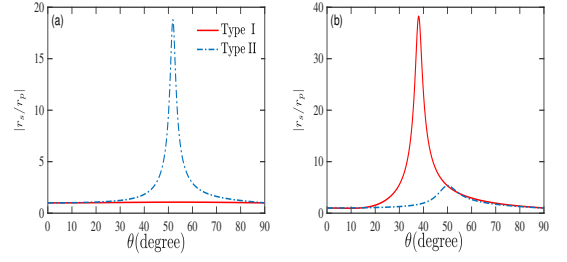


FIG. 3. (Color online) The ratio of reflection coefficients $|r_s/r_p|$ as a function of incident angle θ at different thickness of HMM layer with (a) $d = 200\text{nm}$, and (b) $d = 40\text{nm}$. The parameters are selected with $\lambda = 632.8\text{nm}$, $\rho = 0.5$ and $d_3 = 40\text{nm}$.

where $\gamma_0 = \gamma_{n+1}$ applies for the vacuum before the incidence and after the exit for the designed symmetrical HMM waveguide.

The PSHE shifts of the reflected beam are defined as follows [12]:

$$\delta_{H,V}^{\pm} = \frac{\int \int \tilde{\mathbf{E}}^* i \partial_{k_{ry}} \tilde{\mathbf{E}} dk_{rx} dk_{ry}}{\int \int \tilde{\mathbf{E}}^* \tilde{\mathbf{E}} dk_{rx} dk_{ry}}. \quad (6)$$

Expanding the first-order Taylor series of the Fresnel reflection coefficient $r_{p,s}$ and neglecting the high-order expansion, taking the real part of Eq. (6), combining Eqs. (2) and (5), then the PSHE shifts can be directly calculated as below [12, 42]

$$\delta_H^{\pm} = \mp \frac{k_0 w_0^2 \text{Re}(1 + \frac{r_s}{r_p}) \cot \theta}{k_0^2 w_0^2 + |\frac{\partial(\ln r_p)}{\partial \theta}|^2 + |(1 + \frac{r_s}{r_p}) \cot \theta|^2}, \quad (7)$$

$$\delta_V^{\pm} = \mp \frac{k_0 w_0^2 \text{Re}(1 + \frac{r_p}{r_s}) \cot \theta}{k_0^2 w_0^2 + |\frac{\partial(\ln r_s)}{\partial \theta}|^2 + |(1 + \frac{r_p}{r_s}) \cot \theta|^2}. \quad (8)$$

In the following, we investigate the properties of PSHE shifts by applying Eqs. (7) and (8).

III. RESULTS AND DISCUSSION

It can be seen clearly from Eqs. (7) and (8) that the PSHE shifts mainly depend on the ratio of reflection coefficients $|r_s/r_p|$. Therefore, we first show the behavior of $|r_s/r_p|$, as shown in Fig. 3. Fig. 3(a) presents the ratio of r_s/r_p as a function of the incident angle θ with the thickness of HMM layer $d = 200\text{nm}$, and Fig. 3(b) presents the ratio of $|r_s/r_p|$ as a function of the incident angle θ with the thickness of HMM layer $d = 40\text{nm}$, respectively. The metal sheet is chosen as Ag and its thickness is valued as $d_3 = 40\text{nm}$ in both type I and type II HMM waveguides. It is observed that the type of HMM waveguide and the thickness of HMM layer significantly affect the ratio $|r_s/r_p|$. For the type I HMM waveguide case, the value of ratio $|r_s/r_p|$ is almost the same and does not change nearly in the whole incident

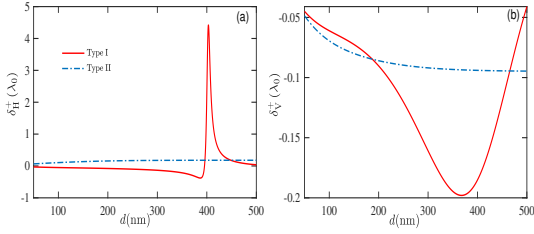


FIG. 4. (Color online) PSHE shift as a function of thickness of HMM layer. (a) Horizontal PSHE shift. The parameters are selected with $\lambda = 632.8\text{nm}$, $\rho = 0.5$, $\theta = 40^\circ$ and $d_3 = 40\text{nm}$. (b) Vertical PSHE shift. Herein, the PSHE shifts are normalized as the incident wavelength.

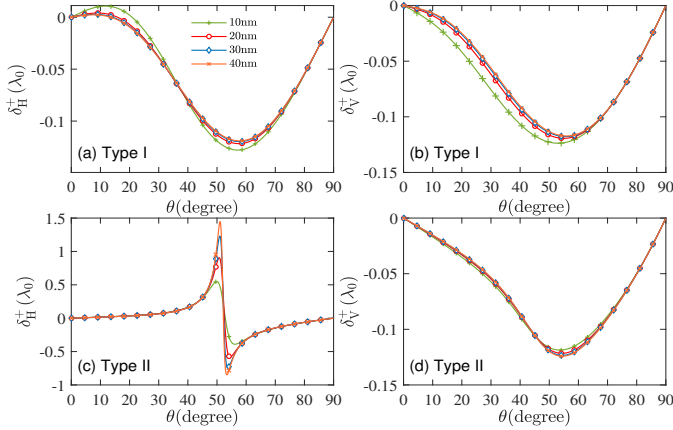


FIG. 5. (Color online) PSHE shift as a function of the incident angle θ with a different metal sheet thickness. The parameters are selected with $\lambda = 632.8\text{nm}$, $\rho = 0.5$ and $d = 200\text{nm}$. (a), (b) type I HMM waveguide. (c), (d) type II HMM waveguide. (a), (c) horizontal PSHE shifts. (b), (d) vertical PSHE shifts. Herein, the PSHE shifts are normalized as the incident wavelength.

angle regions under the case of the thickness of HMM layer with $d = 200\text{nm}$. However, when the thickness of HMM layer increases from 200nm to 400nm , the value of ration $|r_s/r_p|$ first increases rapidly then fall rapidly with increasing the incident angle. The value can arrive at almost 40 multiples. On the contrary, the behavior of $|r_s/r_p|$ in the case of type II HMM waveguide is totally different. When the HMM layer thickness is 200nm , the value of ratio $|r_s/r_p|$ first increases rapidly and then falls rapidly with increases of incident angle θ . The maximum value can be reached to 20 multiplies. However, the value of ration $|r_s/r_p|$ has a slight change under the case of HMM layer thickness 400nm . There is a small fluctuation near the incident angle $\theta = 50^\circ$. From the results of Fig. 3, we can undoubtedly conclude that the PSHE shifts can be tuned by the type of HMM layer and the thickness of HMM layer.

From the above results, we can readily conclude that the type of HMM layer and the thickness of HMM layer

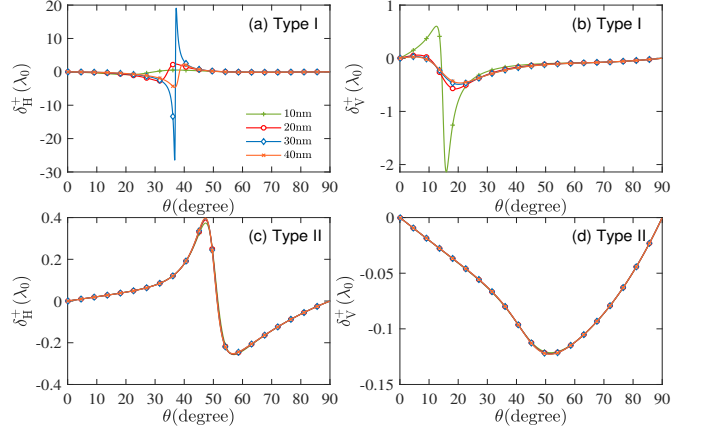


FIG. 6. (Color online) PSHE shift as a function of the incident angle θ with a different metal sheet thickness. The parameters are selected with $\lambda = 632.8\text{nm}$, $\rho = 0.5$ and $d = 400\text{nm}$. (a), (b) type I HMM waveguide. (c), (d) type II HMM waveguide. (a), (c) horizontal PSHE shifts. (b), (d) vertical PSHE shifts. Herein, the PSHE shifts are normalized as the incident wavelength.

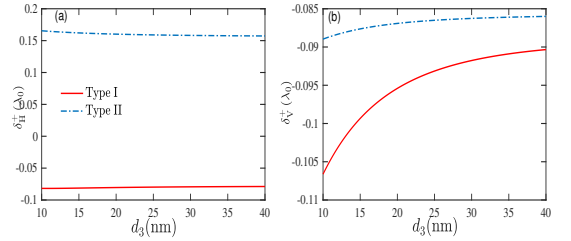


FIG. 7. (Color online) PSHE shift as a function of thickness of HMM layer. The parameters are selected with $\lambda = 632.8\text{nm}$, $\rho = 0.5$, $\theta = 40^\circ$ and $d = 200\text{nm}$. (a) Horizontal PSHE shift. (b) Vertical PSHE shift. Herein, the PSHE shifts are normalized as the incident wavelength.

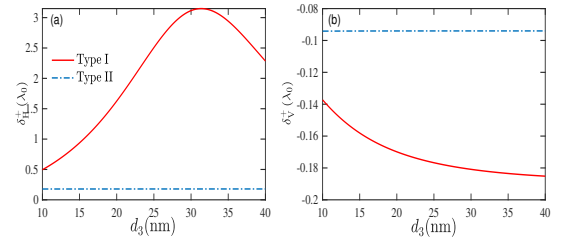


FIG. 8. (Color online) PSHE shift as a function of thickness of HMM layer. The parameters are selected with $\lambda = 632.8\text{nm}$, $\rho = 0.5$, $\theta = 40^\circ$ and $d = 400\text{nm}$. (a) Horizontal PSHE shift. (b) Vertical PSHE shift. Herein, the PSHE shifts are normalized as the incident wavelength.

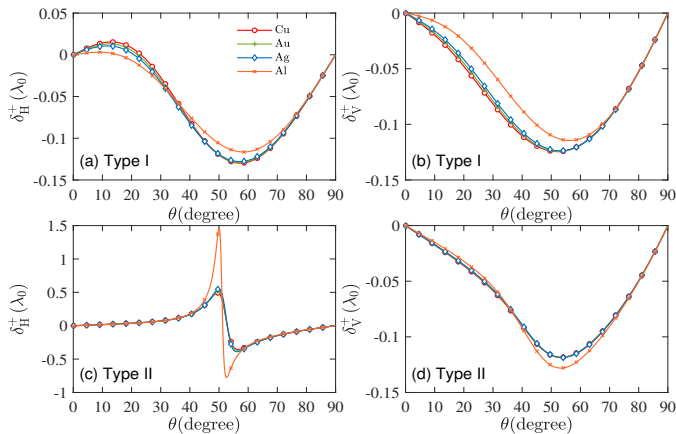


FIG. 9. (Color online) PSHE shift as a function of the incident angle θ with a different type of the metal sheet. The parameters are selected with $\lambda = 632.8\text{nm}$, $\rho = 0.5$ and $d = 200\text{nm}$. (a), (b) type I HMM waveguide. (c), (d) type I HMM waveguide. (a), (c) horizontal PSHE shifts. (b), (d) vertical PSHE shifts. Herein, the PSHE shifts are normalized as the incident wavelength.

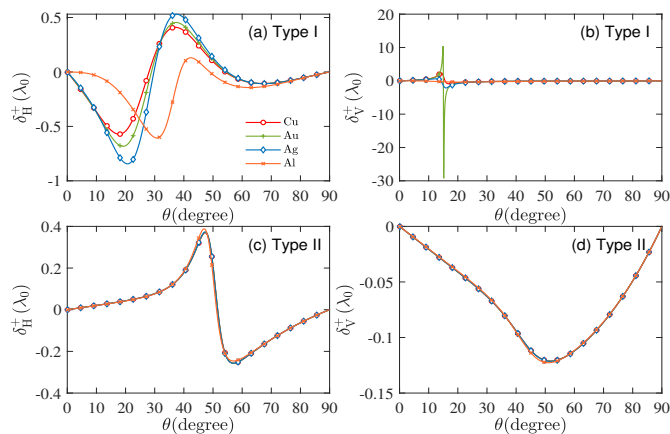


FIG. 10. (Color online) PSHE shift as a function of the incident angle θ with a different type of the metal sheet. The parameters are selected with $\lambda = 632.8\text{nm}$, $\rho = 0.5$ and $d = 400\text{nm}$. (a), (b) type I HMM waveguide. (c), (d) type I HMM waveguide. (a), (c) horizontal PSHE shifts. (b), (d) vertical PSHE shifts. Herein, the PSHE shifts are normalized as the incident wavelength.

significantly alter the PSHE shifts, especially the HMM layer thickness results in two different behavior for type I and type II HMM waveguide. So we proceed to plot the Fig. 4, which shows the PSHE shifts as a function of the thickness of HMM layer. The metal layer is taken as Ag and its thickness is fixed as $d_3 = 40\text{nm}$ and the incident angle is valued as $\theta = 40^\circ$ in all the cases. We can see that the PSHE shifts $\delta_{H,V}$ under the case of type I HMM waveguide is a monotonic function of the thickness of HMM layer d . However, the impact of the thickness of HMM layer is insignificant. Comparing with the case

of type II HMM waveguide, we observe that the horizontal and vertical PSHE shifts under the case of type I HMM waveguide exhibit peak values. Especially for the horizontal PSHE shifts, they are enhanced by more than several times. However, the vertical PSHE shifts are all suppressed by more than several percent.

We further introduce the influence of the metal sheet thickness on the PSHE shifts, seeing Figs. 5 and 6. Fig. 5 presents the case of metal sheet thickness $d_3 = 200\text{nm}$, and Fig. 6 presents the case of metal sheet thickness $d_3 = 400\text{nm}$, respectively. From Fig. 5, we see that only the horizontal PSHE shifts δ_H under the case of type II HMM waveguide have a great change. The horizontal PSHE shifts δ_H has a dramatic change near the incident angle $\theta = 50^\circ$. Moreover, the horizontal PSHE shifts δ_H under the case of type II HMM waveguide increase considerably along with the increases of the metal sheet thickness d_3 . However, both the horizontal and vertical PSHE shifts under the case of type I HMM waveguide, and the vertical PSHE shifts under the case of type I HMM waveguide, are almost the same while varying the metal sheet thickness d_3 . From Fig. 6, we witness that the effect of the metal sheet thickness has a strong impact on both the horizontal and vertical PSHE shifts under the case of type I HMM waveguide while having a slight effect on both the horizontal and vertical shifts under the case of type II HMM waveguide. Especially, the horizontal PSHE shifts under the case of type I HMM waveguide can be enhanced by more than twenty times. Moreover, the effect of the metal sheet thickness on the performance of the horizontal and the vertical PSHE shifts under the case of type I HMM waveguide is quite different. We observe that the horizontal PSHE shifts first increase then decrease, while the vertical PSHE shifts first decrease then increase, by increasing the metal sheet thickness.

Figures 7 and 8 are presented for the PSHE shifts as a function of the metal sheet thickness. Herein, the metal sheet is elected as Ag, and the thickness of HMM layer is fixed to $d = 200\text{nm}$ in Fig. 7 and $d = 400\text{nm}$ in Fig. 8, respectively. The incident angle is fixed as $\theta = 40^\circ$ in these two figures. From Fig. 8, we can see that the horizontal PSHE shifts first increase then decrease by increasing the metal sheet thickness when the HMM layer thickness is planned to $d = 400\text{nm}$ for type I HMM waveguide. However, the horizontal PSHE shifts in both type I and type II HMM waveguide almost stay constant with the increase of the metal sheet thickness. We also observe that the metal sheet thickness has a slight impact on the vertical PSHE shifts whether the thickness of HMM layer $d = 200\text{nm}$ or $d = 400\text{nm}$. It is very interesting to remark that the vertical PSHE shifts for the type I HMM waveguide in the case of $d = 200\text{nm}$ [see Fig. 7(b)] increase while the vertical PSHE shifts in the case of $d = 400\text{nm}$ [see Fig. 8(b)] decrease by increasing the metal sheet thickness.

Finally, we further reveal how the type of metal affects the PSHE shifts, as shown in Figs. 9 and 10. Fig. 9 shows the case of the thickness of HMM layer $d = 200\text{nm}$,

and Fig. 10 shows the case of the thickness of HMM layer $d = 400\text{nm}$, respectively. The four kinds of metal sheet are picked in the work, as the following: Cu with $\varepsilon = -11.6 + 1.69i$, Au with $\varepsilon = -12.8 + 1.4i$, Ag with $\varepsilon = -14.45 + 1.929i$, and Al with $\varepsilon = -56.25 + 20.8i$. All the metal sheet thicknesses are fixed as $d_3 = 40\text{nm}$. The results sound impressive. We can find that the kinds of metal sheets have a slight effect on both the horizontal and vertical PSHE shifts under the case of type I HMM waveguide when the thickness of HMM layer is valued as $d = 200\text{nm}$. However, for the type II HMM waveguide, the effect on the horizontal PSHE shifts is influential, but the effect on the vertical PSHE shifts is tiny. Besides, when the thickness of HMM layer is converted to $d = 400\text{nm}$, the results are different. We can see that the effect is completely reversed. The horizontal and vertical PSHE shifts under the case of type I HMM waveguide are greatly changed by the kinds of the metal sheet, while in the case of type II HMM waveguide the effect of the kinds of the metal sheet is small. Moreover, we observe that the effect on the horizontal PSHE shifts for the type II HMM waveguide largely depends on the real part of the dielectric constant of the metal sheet [see Fig. 9(c)]. This result can also be obtained for the horizontal PSHE shifts under the case of type I HMM waveguide [see Fig. 10(a)].

IV. CONCLUSIONS

In conclusion, we have investigated the features of PSHE shifts when a Gaussian beam impinges from the air to the surface of a three-layered sandwich symmetric HMM waveguide. The waveguide is typically one enclosed metal sheet cladded by two same HMM layers. Two types of HMM waveguide, type I and type II HMM waveguide, are considered in the study. We find that

two ways, alternating subwavelength layer of plasma and dielectric or embedding plasma in the host dielectric matrix, can be employed to realize simultaneously type I and type II HMM. Moreover, the structures engineered in these two ways can exhibit the behavior of effective dielectric, effective metal, I and type II HMM with specific plasma fill fraction and operation wavelength. We show that the ratio of reflectivity, $|r_s/r_p|$, which is directly related to PSHE shifts, is significantly dependent on the type and the thickness of HMM. We also show that the horizontal PSHE shifts can be enhanced by more than several times, especially in the type I HMM waveguide. However, the vertical PSHE shifts are suppressed in both type I and type II HMM waveguide. Besides, we examine the effect of the thickness and the type of the metal sheet on PSHE shifts. We find that it is the thickness of HMM layer to determine how the thickness and the type of the metal sheet affect the PSHE shifts. The influence is weak when the thickness of HMM layer is small. On the contrary, the influence is strong when the thickness of HMM layer is large. Therefore, we can easily conclude that both the type and the thickness of HMM layer are the two most important factors in enhancing and controlling PSHE shifts. Finally, we remark that we only consider the case of a horizontally placed HMM waveguide, while the case of a vertically placed HMM waveguide is beyond the scope of the study. We will study it in the near future.

ACKNOWLEDGMENTS

This work was supported by the Natural Science Foundation of China (11975175 and 11575135) and the Fundamental Research Funds for the Central Universities (WUT: 2020IB021).

-
- [1] K. Y. Bliokh and Y. P. Bliokh, Conservation of angular momentum, transverse shift, and spin hall effect in reflection and refraction of an electromagnetic wave packet, *Physical Review Letters* **96**, 073903 (2006).
 - [2] K. Y. Bliokh, A. Niv, V. Kleiner, and E. Hasman, Geometrodynamics of spinning light, *Nature Photonics* **2**, 748 (2008).
 - [3] M. Onoda, S. Murakami, and N. Nagaosa, Hall effect of light, *Physical Review Letters* **93**, 083901 (2004).
 - [4] X. Ling, X. Zhou, K. Huang, Y. Liu, C. W. Qiu, H. Luo, and S. Wen, Recent advances in the spin hall effect of light, *Reports on Progress in Physics* **80**, 066401 (2017).
 - [5] O. Hosten and P. Kwiat, Observation of the spin hall effect of light via weak measurements, *Science* **319**, 787 (2008).
 - [6] Y. Qin, Y. Li, H. He, and Q. Gong, Measurement of spin hall effect of reflected light, *Optics Letters* **34**, 2551 (2009).
 - [7] K. Y. Bliokh, A. Y. Bekshaev, A. G. Kofman, and F. Nori, Photon trajectories, anomalous velocities and weak measurements: a classical interpretation, *New Journal of Physics* **15**, 073022 (2013).
 - [8] X. Zhou, L. Sheng, and X. Ling, Photonic spin hall effect enabled refractive index sensor using weak measurements, *Scientific Reports* **8**, 1221 (2018).
 - [9] L.-J. Kong, X.-L. Wang, S.-M. Li, Y. Li, J. Chen, B. Gu, and H.-T. Wang, Spin hall effect of reflected light from an air-glass interface around the brewster's angle, *Applied Physics Letters* **100**, 071109 (2012).
 - [10] W. Zhu and W. She, Enhanced spin hall effect of transmitted light through a thin epsilon-near-zero slab, *Optics Letters* **40**, 2961 (2015).
 - [11] X. Qiu, Z. Zhang, L. Xie, J. Qiu, F. Gao, and J. Du, Incident-polarization-sensitive and large in-plane-photonic-spin-splitting at the brewster angle, *Optics Letters* **40**, 1018 (2015).
 - [12] Z. Qin, Q. Liu, C. Yue, and Y. Lang, Modified model of photonic spin hall effect of gaussian beam reflected from a dielectric interface, *Applied Physics Express* **12**, 062008 (2019).

- [13] A. Aiello, N. Lindlein, C. Marquardt, and G. Leuchs, Transverse angular momentum and geometric spin hall effect of light, *Physical Review Letters* **103**, 100401 (2009).
- [14] X. Zhou, X. Ling, H. Luo, and S. Wen, Identifying graphene layers via spin hall effect of light, *Applied Physics Letters* **101**, 251602 (2012).
- [15] X. Ling, X. Zhou, and X. Yi, Geometric spin hall effect of light with inhomogeneous polarization, *Optics Communications* **383**, 412 (2017).
- [16] X. Yin, Z. Ye, J. Rho, Y. Wang, and X. Zhang, Photonic spin hall effect at metasurfaces, *Science* **339**, 1405 (2013).
- [17] Y. Liu, Y. Ke, H. Luo, and S. Wen, Photonic spin hall effect in metasurfaces: a brief review, *Nanophotonics* **6**, 51 (2017).
- [18] K. Chaudhuri, A. Shaltout, D. Shah, U. Guler, A. Dutta, V. M. Shalaev, and A. Boltasseva, Photonic spin hall effect in robust phase gradient metasurfaces utilizing transition metal nitrides, *ACS Photonics* **6**, 99 (2019).
- [19] J. Li, T. Tang, L. Luo, and J. Yao, Enhancement and modulation of photonic spin hall effect by defect modes in photonic crystals with graphene, *Carbon* **134**, 293 (2018).
- [20] W. Chen, Y. Liu, and B. Guo, Tunable modulation of photonic spin hall effect owing to the defect mode in one-dimensional photonic crystal with plasma, *Physics of Plasmas* **26**, 052110 (2019).
- [21] Y. L. Liu, W. C. Chen, and B. Guo, Magneto-optical effects on the properties of the photonic spin hall effect owing to the defect mode in photonic crystals with plasma, *AIP Advances* **9**, 075111 (2019).
- [22] B. Xie, G. Su, H.-F. Wang, F. Liu, L. Hu, S.-Y. Yu, P. Zhan, M.-H. Lu, Z. Wang, and Y.-F. Chen, Higher-order quantum spin hall effect in a photonic crystal, *Nature Communications* **11**, 3768 (2020).
- [23] C. Gao and B. Guo, Enhancement and tuning of spin hall effect of light in plasma metamaterial waveguide, *Physics of Plasmas* **24**, 093520 (2017).
- [24] C. Gao and B. Guo, Tunable the spin hall effect of light with graphene metamaterial, *Optik* **158**, 850 (2018).
- [25] H. Zheng, C. Gao, M. Gao, and B. Guo, Tunability of spin hall effect of light with semiconductor metamaterial based on magneto-optical effects, *Optical and Quantum Electronics* **50**, 273 (2018).
- [26] Z. Guo, H. Jiang, Y. Long, K. Yu, J. Ren, C. Xue, and H. Chen, Photonic spin hall effect in waveguides composed of two types of single-negative metamaterials, *Scientific Reports* **7**, 7742 (2017).
- [27] T. Tang, J. Li, Y. Zhang, C. Li, and L. Luo, Spin hall effect of transmitted light in a three-layer waveguide with lossy epsilon-near-zero metamaterial, *Optics Express* **24**, 28113 (2016).
- [28] H. Chen, S. Zhou, G. Rui, and Q. Zhan, Magnified photonic spin-hall effect with curved hyperbolic metamaterials, *Journal of Applied Physics* **124**, 233104 (2018).
- [29] O. Takayama, J. Sukham, R. Malureanu, A. V. Lavrinenko, and G. Puentes, Photonic spin hall effect in hyperbolic metamaterials at visible wavelengths, *Optics Letters* **43**, 4602 (2018).
- [30] P. V. Kapitanova, P. Ginzburg, F. J. Rodríguez-Fortuño, D. S. Filonov, P. M. Voroshilov, P. A. Belov, A. N. Podubny, Y. S. Kivshar, G. A. Wurtz, and A. V. Zayats, Photonic spin hall effect in hyperbolic metamaterials for polarization-controlled routing of subwavelength modes, *Nature Communications* **5**, 3226 (2014).
- [31] Y.-Y. Fu, Y. Fei, D.-X. Dong, and Y.-W. Liu, Photonic spin hall effect in pt symmetric metamaterials, *Frontiers of Physics* **14**, 62601 (2019).
- [32] M. Kim, D. Lee, T. H. Kim, Y. Yang, H. J. Park, and J. Rho, Observation of enhanced optical spin hall effect in a vertical hyperbolic metamaterial, *ACS Photonics* **6**, 2530 (2019).
- [33] W.-Q. Zhang, M.-X. Gao, and B. Guo, Tunable modulation of photonic spin hall effect by using a prism-coupling waveguide with hyperbolic metamaterials, *Journal of the Optical Society of America B* **37**, 3777 (2020).
- [34] P. Wang, S. Guo, Q. Wang, H. Zhang, and D. Zhang, Non-reciprocity in the spin hall effect based on multilayer magnetized plasma, *Applied Optics* **60**, 1834 (2021).
- [35] P. Wang, B. Wan, Q. Wang, H. Zhang, and D. Zhang, Research on the performance of the spin hall effect of light based on a magnetized plasma layered structure, *Journal of the Optical Society of America B* **38**, 562 (2021).
- [36] P.-X. Wang, B.-F. Wan, H.-M. Peng, Y. Ma, H.-F. Zhang, and D. Zhang, Theoretical research on enhancement and adjustment of spin hall effect of light based on insb, *Optical and Quantum Electronics* **53**, 113 (2021).
- [37] X. Zhou, X. Lin, Z. Xiao, T. Low, A. Alù, B. Zhang, and H. Sun, Controlling photonic spin hall effect via exceptional points, *Physical Review B* **100**, 115429 (2019).
- [38] G. Jia, G. Li, Y. Zhou, X. Miao, and X. Zhou, Landau quantisation of photonic spin hall effect in monolayer black phosphorus, *Nanophotonics* **9**, 225 (2019).
- [39] G. Y. Jia, Z. X. Huang, Q. Y. Ma, and G. Li, Photonic spin hall effect on the surfaces of type-i and type-ii weyl semimetals, *Nanophotonics* **9**, 715 (2020).
- [40] X. Jiang, J. Tang, Z. Li, Y. Liao, L. Jiang, X. Dai, and Y. Xiang, Enhancement of photonic spin hall effect via bound states in the continuum, *Journal of Physics D: Applied Physics* **52**, 045401 (2018).
- [41] W. Li, J. Liu, Y. Gao, K. Zhou, and S. Liu, Photonic spin hall effect on an ellipsoidal rayleigh particle in scattering far-field, *Optics Express* **27**, 28194 (2019).
- [42] R.-G. Wan and M. S. Zubairy, Controlling photonic spin hall effect based on tunable surface plasmon resonance with an n -type coherent medium, *Physical Review A* **101**, 033837 (2020).
- [43] L. Ferrari, C. Wu, D. Lepage, X. Zhang, and Z. Liu, Hyperbolic metamaterials and their applications, *Progress in Quantum Electronics* **40**, 1 (2015).
- [44] P. Shekhar, J. Atkinson, and Z. Jacob, Hyperbolic metamaterials: fundamentals and applications, *Nano Convergence* **1**, 14 (2014).
- [45] T. C. Choy, *Effective medium theory: principles and applications* (Oxford University, 1999).
- [46] J. Elser, R. Wangberg, V. A. Podolskiy, and E. E. Narimanov, Nanowire metamaterials with extreme optical anisotropy, *Applied Physics Letters* **89**, 261102 (2006).
- [47] C. L. Cortes, W. Newman, S. Molesky, and Z. Jacob, Corrigendum: Quantum nanophotonics using hyperbolic metamaterials (2012 j. opt. 14 063001), *Journal of Optics* **16**, 129501 (2014).
- [48] P. Yeh, *Optical Waves in Layered Media* (John Wiley and Sons, Singapore, 1991).

Figures

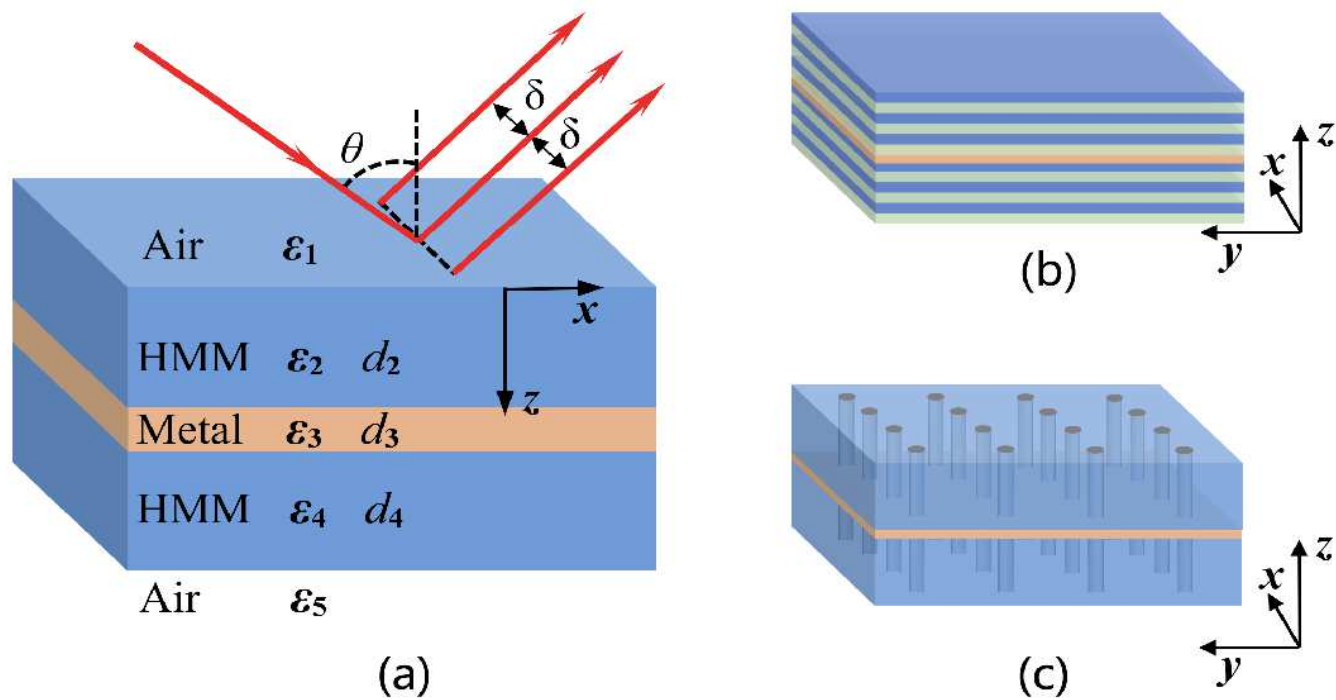


Figure 1

(Color online) (a) Schematic diagram of PSHE of the reflected light in the symmetric HMM waveguide. (b) HMM engineered through multilayer realization consists of alternating subwavelength layers of plasma and dielectric. (c) HMM engineered through embedding plasma in a host dielectric matrix.

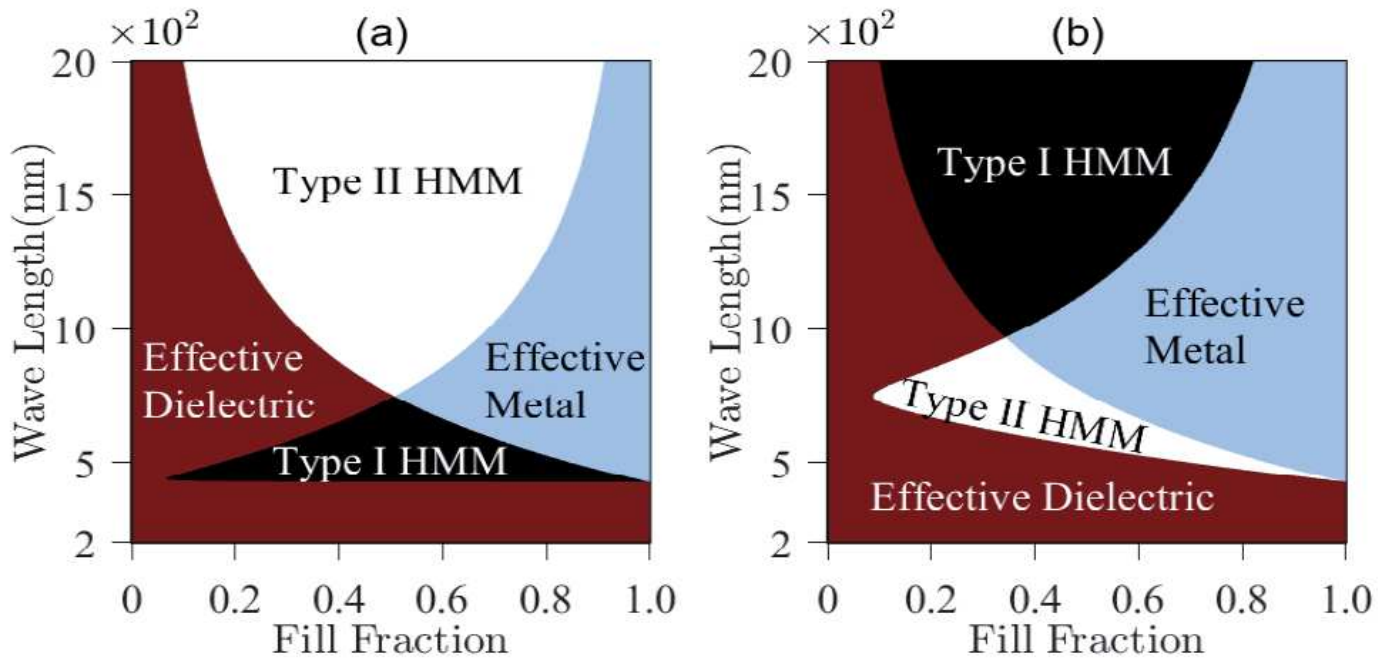


Figure 2

(Color online) The engineered composite can behave as an effective dielectric, effective metal, type I HMM or type II HMM depending on the wavelength and fill fraction of the plasma. Optical phase diagrams for (a) one-dimensional HMM, and (b) Two-dimensional HMM.

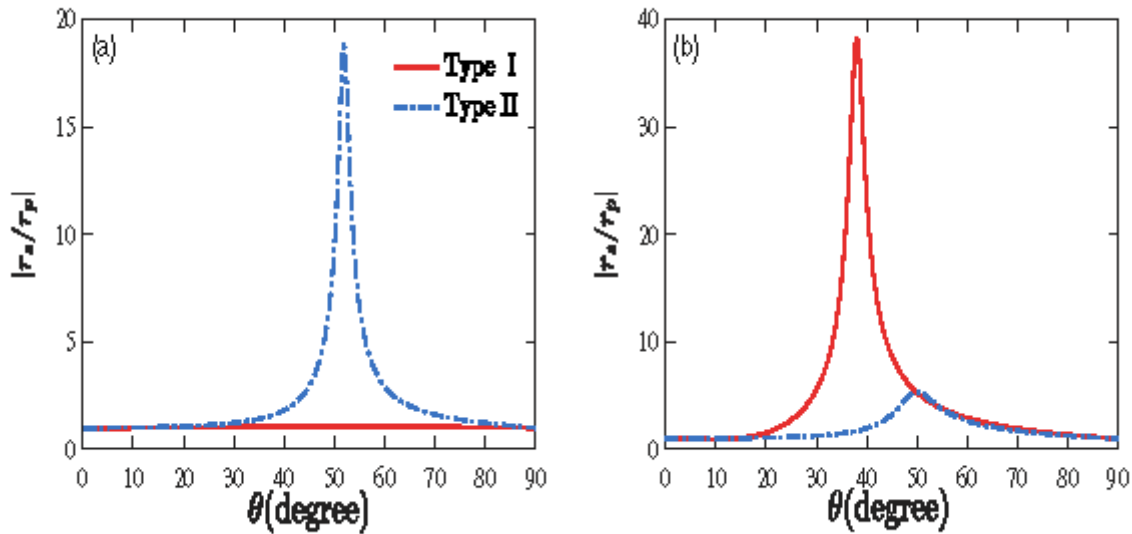


Figure 3

(Color online) The ratio of reflection coefficients $|r_s/r_p|$ as a function of incident angle θ at different thickness of HMM layer with (a) $d = 200\text{nm}$, and (b) $d_4 = 40\text{nm}$. The parameters are selected with $\lambda = 632.8\text{nm}$, $\rho = 0.5$ and $d_3 = 40\text{nm}$.

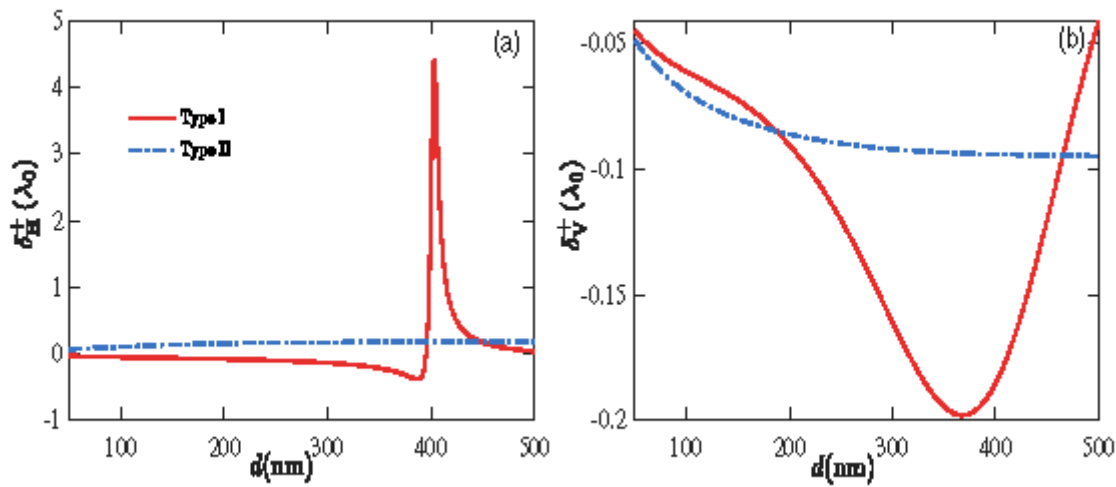


Figure 4

(Color online) PSHE shift as a function of thickness of HMM layer. (a) Horizontal PSHE shift. The parameters are selected with $\lambda = 632.8$ nm, $\rho = 0.5$, $\theta = 40^\circ$ and $d_3 = 40$ nm. (b) Vertical PSHE shift. Herein, the PSHE shifts are normalized as the incident wavelength.

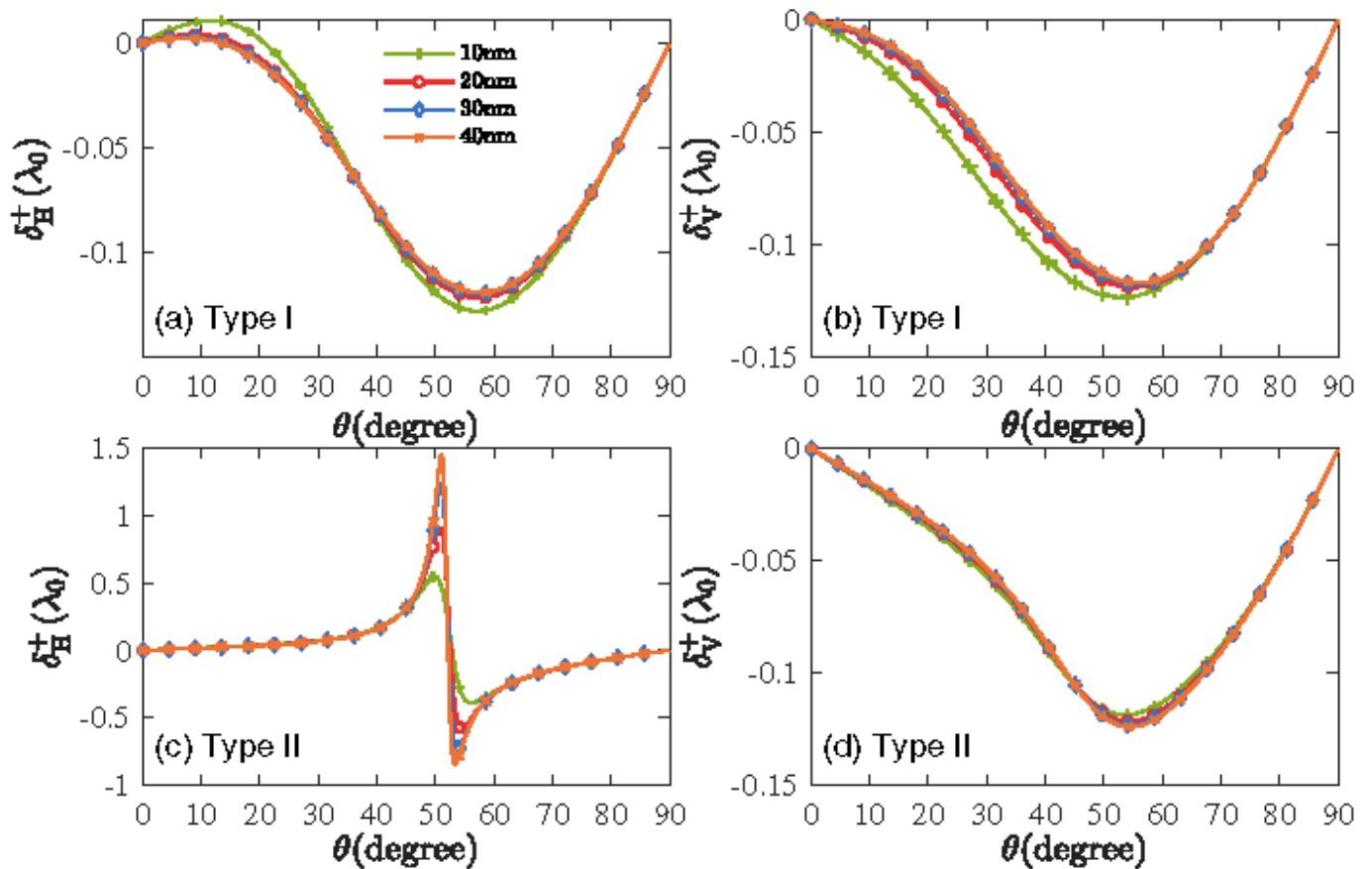


Figure 5

(Color online) PSHE shift as a function of the incident angle θ with a different metal sheet thickness. The parameters are selected with $\lambda = 632.8\text{nm}$, $\rho = 0.5$ and $d = 200\text{nm}$. (a), (b) type I HMM waveguide. (c), (d) type I HMM waveguide. (a), (c) horizontal PSHE shifts. (b), (d) vertical PSHE shifts. Herein, the PSHE shifts are normalized as the incident wavelength.

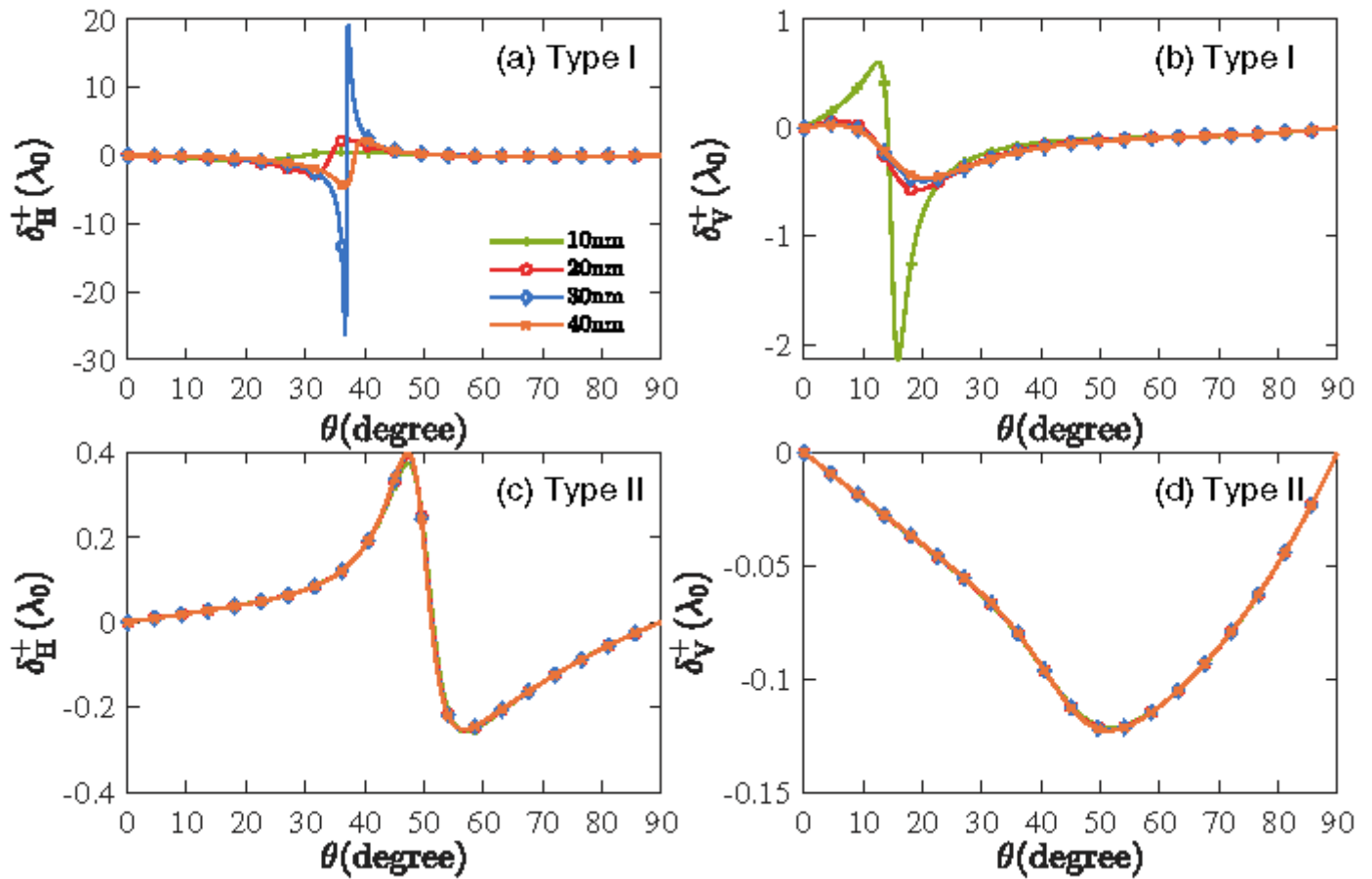


Figure 6

(Color online) PSHE shift as a function of the incident angle θ with a different metal sheet thickness. The parameters are selected with $\lambda = 632.8\text{nm}$, $\rho = 0.5$ and $d = 400\text{nm}$. (a), (b) type I HMM waveguide. (c), (d) type I HMM waveguide. (a), (c) horizontal PSHE shifts. (b), (d) vertical PSHE shifts. Herein, the PSHE shifts are normalized as the incident wavelength.

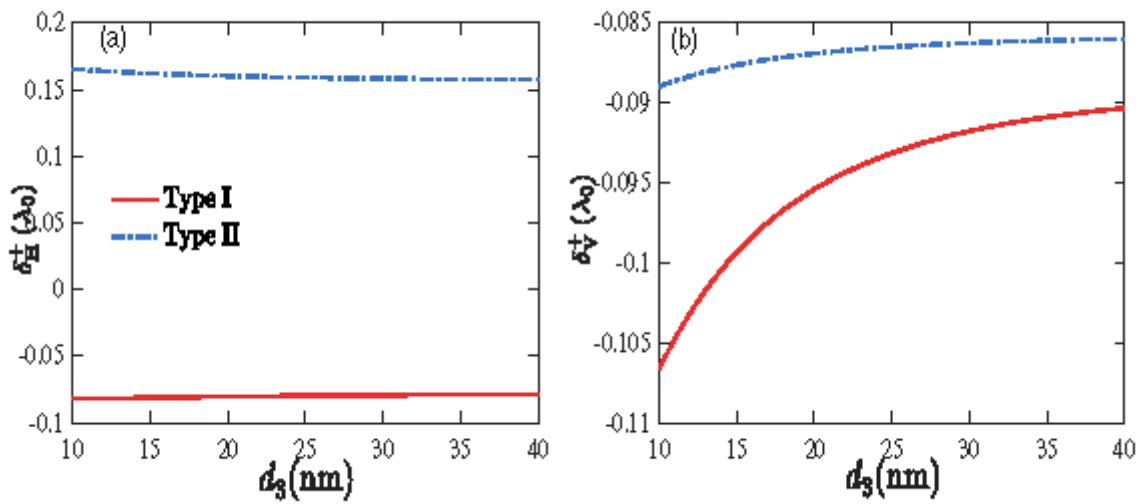


Figure 7

(Color online) PSHE shift as a function of thickness of HMM layer. The parameters are selected with $\lambda = 632.8$ nm, $\rho = 0.5$, $\theta = 40^\circ$ and $d = 200$ nm. (a) Horizontal PSHE shift. (b) Vertical PSHE shift. Herein, the PSHE shifts are normalized as the incident wavelength.

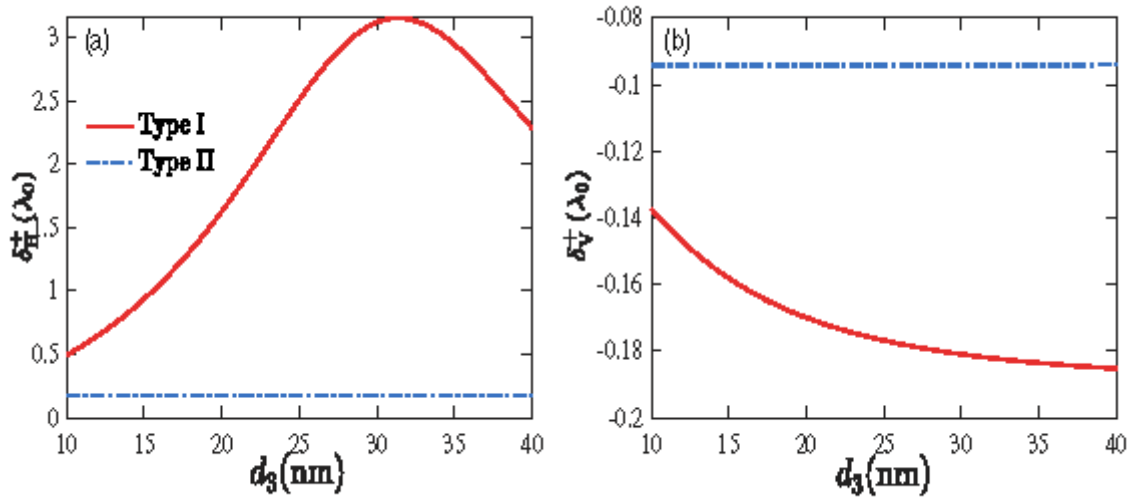


Figure 8

(Color online) PSHE shift as a function of thickness of HMM layer. The parameters are selected with $\lambda = 632.8$ nm, $\rho = 0.5$, $\theta = 40^\circ$ and $d = 400$ nm. (a) Horizontal PSHE shift. (b) Vertical PSHE shift. Herein, the PSHE shifts are normalized as the incident wavelength.

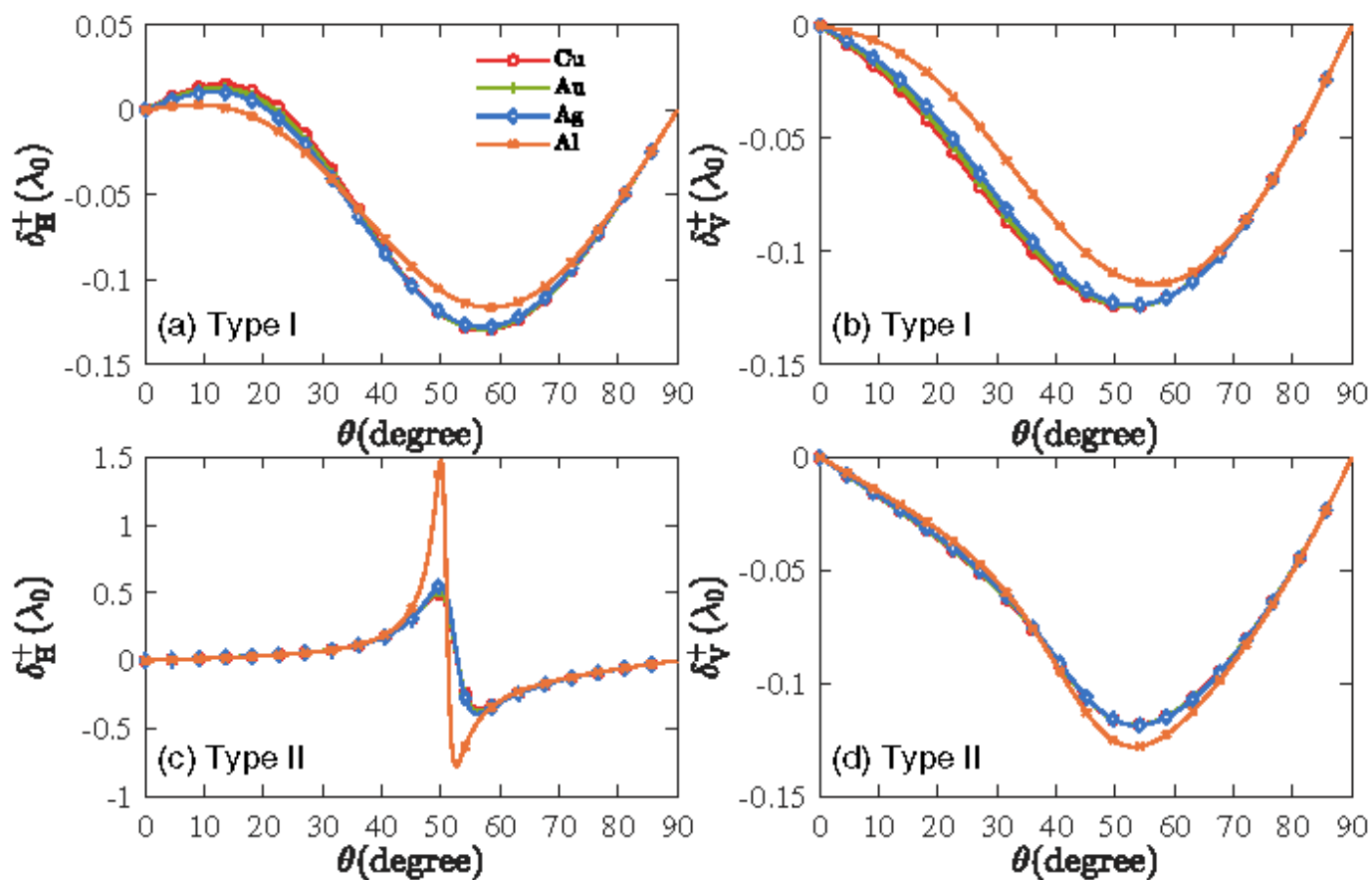


Figure 9

(Color online) PSHE shift as a function of the incident angle θ with a different type of the metal sheet. The parameters are selected with $\lambda = 632.8\text{nm}$, $\rho = 0.5$ and $d = 200\text{nm}$. (a), (b) type I HMM waveguide. (c), (d) type II HMM waveguide. (a), (c) horizontal PSHE shifts. (b), (d) vertical PSHE shifts. Herein, the PSHE shifts are normalized as the incident wavelength.

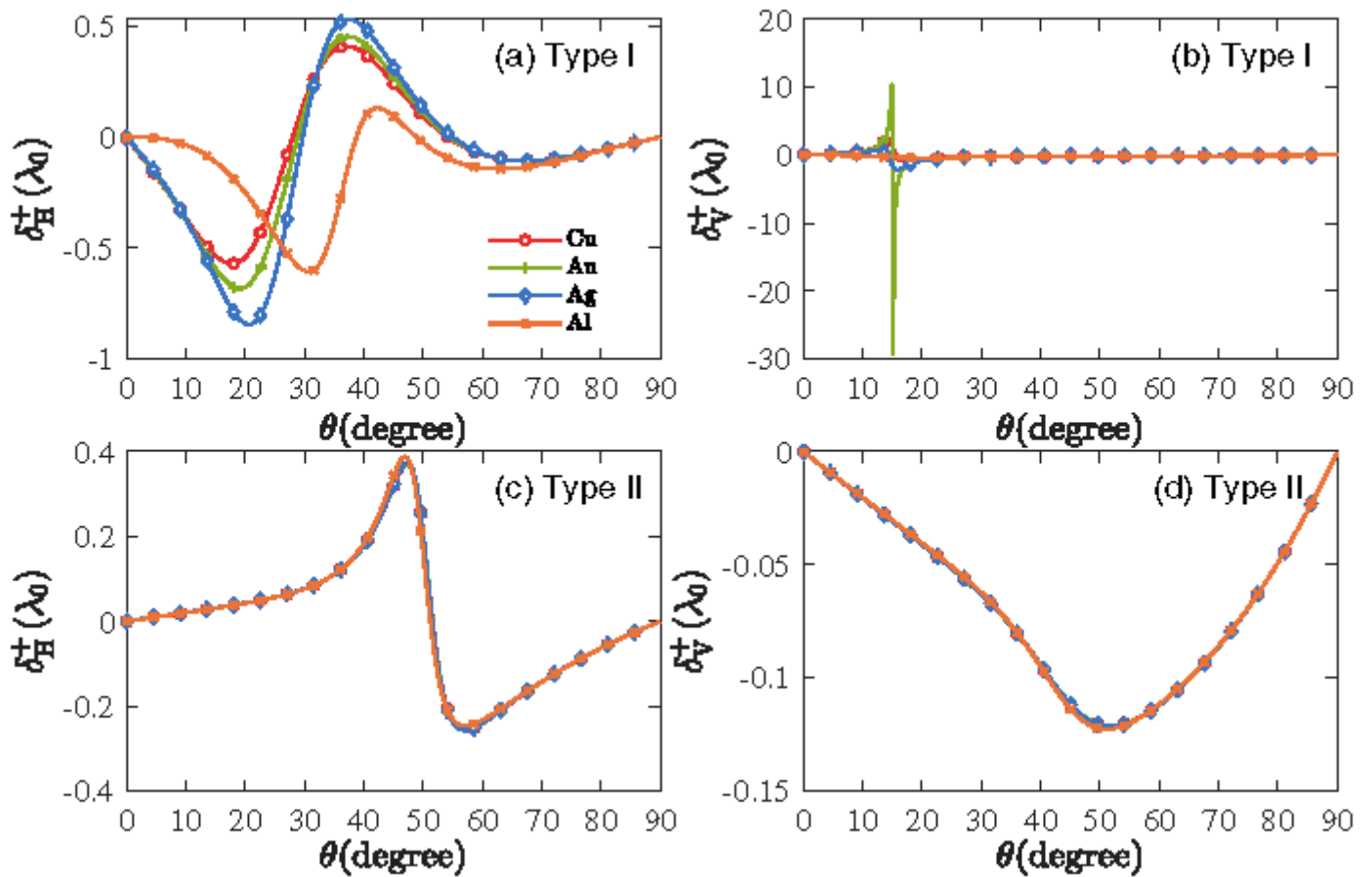


Figure 10

(Color online) PSHE shift as a function of the incident angle θ with a different type of the metal sheet. The parameters are selected with $\lambda = 632.8\text{nm}$, $\rho = 0.5$ and $d = 400\text{nm}$. (a), (b) type I HMM waveguide. (c), (d) type II HMM waveguide. (a), (c) horizontal PSHE shifts. (b), (d) vertical PSHE shifts. Herein, the PSHE shifts are normalized as the incident wavelength.